JACS
JOURNAL OF THE AMERICAN CHEMICAL SOCIETY
Article
Cite This: J. Am. Chem. Soc. XXXX, XXX, XXX−XXX
pubs.acs.org/JACS

Binding Site Diversity Promotes CO_2 Electroreduction to Ethanol

Yuguang C. Li,[†,∥] Ziyun Wang,[†,∥] Tiange Yuan,[‡] Dae-Hyun Nam,[†] Mingchuan Luo,[†] Joshua Wicks,[†] Bin Chen,[†] Jun Li,[†,§] Fengwang Li,[†] F. Pelayo García de Arquer,[†] Ying Wang,[†] Cao-Thang Dinh,[†] Oleksandr Voznyy,[‡] David Sinton,[§] and Edward H. Sargent*[,†]

[†]Department of Electrical and Computer Engineering, University of Toronto, 35 St. George Street, Toronto, Ontario M5S 1A4, Canada

[‡]Department of Physical and Environmental Sciences, University of Toronto, Scarborough, 1065 Military Trail, Toronto, Ontario M1C 1A4, Canada

[§]Department of Mechanical and Industrial Engineering, University of Toronto, 5 King's College Road, Toronto, Ontario M5S 3G8, Canada

Supporting Information

ABSTRACT: The electrochemical reduction of CO_2 has seen many record-setting advances in C_2 productivity in recent years. However, the selectivity for ethanol, a globally significant commodity chemical, is still low compared to the selectivity for products such as ethylene. Here we introduce diverse binding sites to a Cu catalyst, an approach that destabilizes the ethylene reaction intermediates and thereby promotes ethanol production. We develop a bimetallic Ag/Cu catalyst that implements the proposed design toward an improved ethanol catalyst. It achieves a record Faradaic efficiency of 41% toward ethanol at 250 mA/cm^2 and −0.67 V vs RHE, leading to a cathodic-side (half-cell) energy efficiency of 24.7%. The new catalysts exhibit an in situ Raman spectrum, in the region associated with CO stretching, that is much broader than that of pure Cu controls, a finding we account for via the diversity of binding configurations. This physical picture, involving multisite binding, accounts for the enhanced ethanol production for bimetallic catalysts, and presents a framework to design multimetallic catalysts to control reaction paths in CO_2 reductions toward desired products.

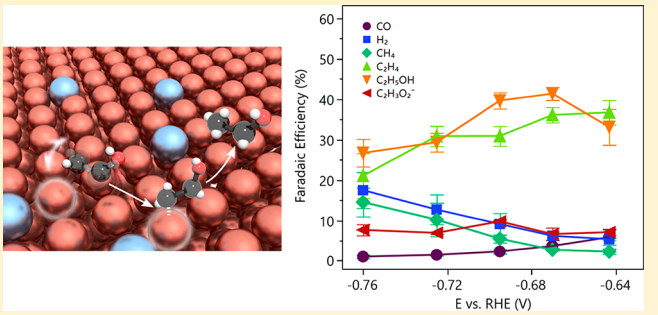

INTRODUCTION

Among the major products from the CO_2 reduction reaction (CO_2RR), CO and formate have each been achieved with close to unity current efficiency.[1,2] C_{2+} products, including ethylene and ethanol, offer the prospect of higher energy density and market value compared to C_1.[3] Further progress in C_{2+} selectivity will help to make these CO_2RR technologies more economically competitive.

Ethylene has recently been reported with remarkable efficiency and stability.[4] Ethanol, on the other hand, has so far seen much lower selectivity in CO_2RR. Ethanol is a liquid fuel with a high energy density (26.8 MJ/kg) and also functions as a widely used intermediate in chemical synthesis. As a liquid product, it is readily stored and transported and thus is used as an additive to gasoline. Achieving a high current density and improving the Faradaic efficiency (FE) for ethanol production are important aims to advance CO_2RR from its initial promise as a renewable chemical feedstock and toward impact on the larger renewable fuels sector.

Copper and copper-based alloys are so far the only catalysts that generate C_2 chemicals as major products and produce ethanol at a significant rate of productivity.[5,6] Carbon-based catalysts have been reported to achieve promising ethanol FE, but at low sub-5 mA/cm^2 current densities.[7,8] Cu-based catalysts generate more ethylene than ethanol, typically in the range of 2× to 3× times higher.[9−11]

Ethylene and ethanol share many intermediates and both are 12-electron reduced products,[12−14] yet the competing reaction pathways, and differences in the ratios among these two products, have yet to be fully understood. Handoko et al. have suggested that the reaction paths for ethylene and ethanol are distinct, and that oxide-derived Cu is more favorable for ethanol over ethylene in view of its higher density of Cu^+ sites.[15] Hahn et al. studied the different crystal facets of single crystal Cu and found that the undercoordinated Cu surface is more favorable for oxygenate production.[16]

While the reasons underpinning the observation that ethanol is produced with lower Faradaic efficiencies than ethylene remain the subject of debate, many reports in the past several years have focused on optimizing the ethanol efficiency (Table S1). Strategies have included introducing compressive strain,[9] the use of tandem catalysts,[17,18] morphological control,[19,20] amorphous catalysts,[21] vacancy engineering[22] and substrate

Received: March 18, 2019
Published: May 8, 2019

DOI: 10.1021/jacs.9b02945
J. Am. Chem. Soc. XXXX, XXX, XXX−XXX

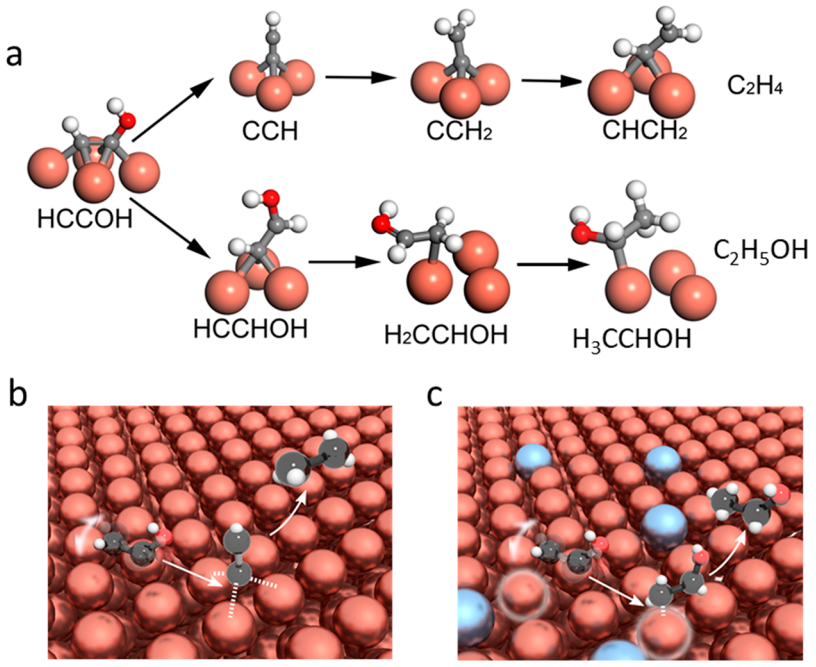

Figure 1. Catalyst design principle. (a) Reaction paths for ethylene vs ethanol on a Cu(111) surface. Binding illustration for Cu (b) and Ag/Cu (c) catalyst to produce ethylene and ethanol, respectively. Due to the introduction of Ag atom on the Cu surface, the coordination sites for ethylene intermediates are disrupted, and thus leads to improved ethanol production.

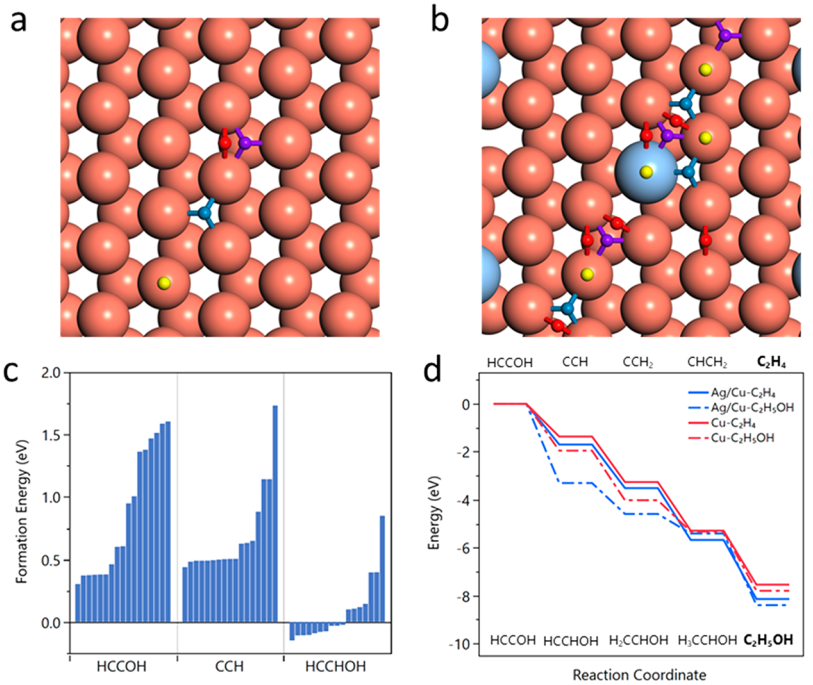

Figure 2. Formation energy of intermediates. (a,b) Binding site configurations for Cu (a) and Ag/Cu (b) catalysts. (c) Formation energy for *HCCOH (prebranch), *CCH (ethylene path), and *HCCHOH (ethanol path) on the Ag/Cu. The intermediates toward ethylene are destabilized. (d) Energy profiles of all intermediates toward ethylene and ethanol on Cu and Ag/Cu catalysts. Intermediates for all the binding sites on Cu and Ag/Cu are calculated and then averaged. The energy profiles are corrected to −0.7 V vs RHE according to the computational hydrogen electrode.

electronic effects.[23] The best ethanol FE reached 30% and up to 300 mA/cm^2 of current density.[10,17,22]

Herein we sought an approach to catalyst design that would tune CO_2RR toward ethanol based on an understanding of reaction intermediates. Building on the ethanol vs ethylene pathway study recently reported by Goddard et al.,[12,24] we used density functional theory (DFT) to examine the stabilities of key intermediates. When we introduced, in silico, an inert element onto the Cu surface, the intermediates in the ethylene path were seen to destabilize, while the ethanol path improved.

Experimentally, we verified this concept by synthesizing Ag/Cu catalysts that achieve an ethanol FE of 41% at a current

DOI: 10.1021/jacs.9b02945
J. Am. Chem. Soc. XXXX, XXX, XXX−XXX

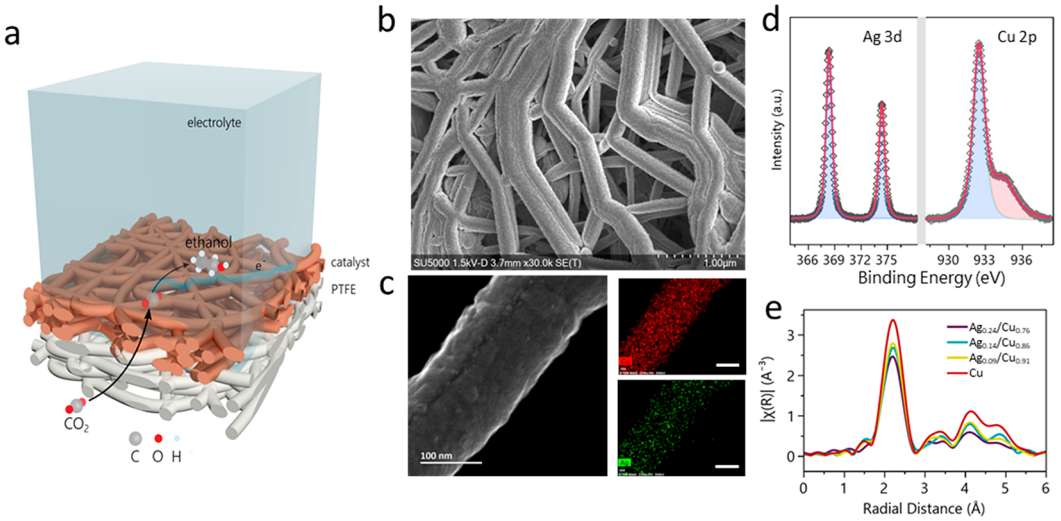

Figure 3. Structural and compositional analysis of the Ag/Cu catalysts. (a) Schematic illustration of the catalyst electrode, consisting of the PTFE substrate and catalyst. CO_2 gas diffuses through the PTFE and reaches the catalyst-electrolyte interface to generate ethanol. (b) SEM image of the as-prepared $Ag_{0.14}/Cu_{0.86}$ catalyst on PTFE. (c) STEM image and EDX mapping of the $Ag_{0.14}/Cu_{0.86}$ catalyst showing uniform Cu and Ag distribution. All scale bars are 100 nm. (d) XPS spectra of Ag 3d and Cu 2p for the $Ag_{0.14}/Cu_{0.86}$ catalyst. (e) In situ Cu K edge EXAFS of Cu, $Ag_{0.09}/Cu_{0.91}$, $Ag_{0.14}/Cu_{0.86}$, and $Ag_{0.24}/Cu_{0.76}$. Coordination number for the Cu−Cu bond decreases from 12 (pure Cu) to 10.7, 10.2, and 9.6, respectively, for the three Ag samples.

density of 250 mA/cm^2 in a flow cell reactor. We also carried out morphological characterization that elucidated the composition and nature of the surface, and used in situ XAS, Raman spectroscopy, and electrochemical measurements to confirm the multibinding site mechanism.

RESULTS AND DISCUSSION

Ethylene and ethanol share similar initial reaction pathways[12−14]—starting from the *CO dimerization step, followed by several steps of protonation and a dehydration, and up to the point at which *HCCOH is formed. The reaction paths for ethylene and ethanol branch off from *HCCOH to the final products, and this branching is driven by the relative stabilities of the surface intermediates.[12,13,24] Prior reports have consistently observed that the Cu surface favors ethylene over ethanol. We sought herein a design strategy to modify the Cu surface and switch the reaction from ethylene to ethanol.

Figure 1a shows the reaction paths for ethylene and ethanol on Cu(111), starting from *HCCOH. Reaction intermediates for ethylene are more unsaturated compared to those for ethanol. This result agrees with previous reports that ethylene is favored on highly coordinated surface.[16,25]

We therefore posited that, by introducing a second element that has weaker bonding ability to carbon than copper, one could lower the likelihood of ethylene intermediates forming on the catalyst surface, as illustrated in Figure 1b and c. This would destabilize the ethylene reaction path and enhance the selectivity for ethanol. From the CO_2RR volcano plot,[26] only Ag and Au are on the weaker bonding side of Cu. Thus, we carried out DFT calculations to investigate this notion, introducing silver element onto Cu(111) in a 3 × 3 unit cell, leading to an 11% surface ratio of silver.

There are four distinct classes of binding sites (Figure 2a) on Cu(111), whereas there are 16 different binding sites (Figure 2b) on Ag-doped Cu(111). The sites close to Ag are more Ag-like, while Cu sites far from Ag behave more akin to pure Cu. The stabilities of intermediates on the various binding sites in both pathways will determine the overall selectivity of the catalyst. With the introduction of Ag, DFT calculations show that the CO_2 activation occurs mostly still on the Cu sites (Figure S1). We then proceed to calculate the formation energy of each of the intermediates along the ethylene and ethanol pathways on the Cu and Ag/Cu surfaces. Figure 2c compares *HCCOH (prebranching), *CCH (ethylene pathway), and *HCCHOH (ethanol pathway) formation energies on the Ag/Cu surface. Each bar represents one of the binding configurations. The formation energies (Table S2) of both *HCCOH and *CCH vary across a wider range compared to that of *HCCHOH—i.e., *HCCHOH is less sensitive to the introduction of Ag. Figure 2d further shows the energy profiles of the intermediates on the ethylene and ethanol paths for both the Cu and the Ag/Cu surfaces, at −0.7 V vs RHE (Table S3−S5).[27] The intermediates along the ethanol pathway become more favorable on the Ag/Cu surface compared to those on pure Cu(111).

Thus, by introducing multiple bind sites on the Cu surface, especially ones having weaker catalyst:carbon bonding ability, the highly coordinated chemical environment is disrupted and the ethylene reaction path is destabilized. The approach is predicted to tune the CO_2RR reaction to achieve better ethanol production.

In light of these predictions, we fabricated via cosputtering a suite of Ag/Cu catalysts having different Ag−Cu ratios.[10,28] Pure Cu catalyst controls were also prepared using the same sputtering approach. All catalysts were deposited on a PTFE substrate, an approach that increases gas diffusion and prevents electrode flooding.[4,29] The full catalyst electrode is depicted in Figure 3a. Scanning electron microscope (SEM) images (Figure 3b and Figure S2−S4) reveal that the catalyst covers the PTFE fiber and preserves the web-like morphology of the PTFE substrate. Energy dispersive X-ray spectroscopy (EDX) (Figure S2−S4) mapping shows that the Ag and Cu elements are evenly distributed. At higher magnification with scanning transmission electron microscopy (STEM) (Figure 3c and Figure S5), some surface roughness is observed, but the surface remains relatively featureless at the nanoscale. EDX from

DOI: 10.1021/jacs.9b02945
J. Am. Chem. Soc. XXXX, XXX, XXX−XXX

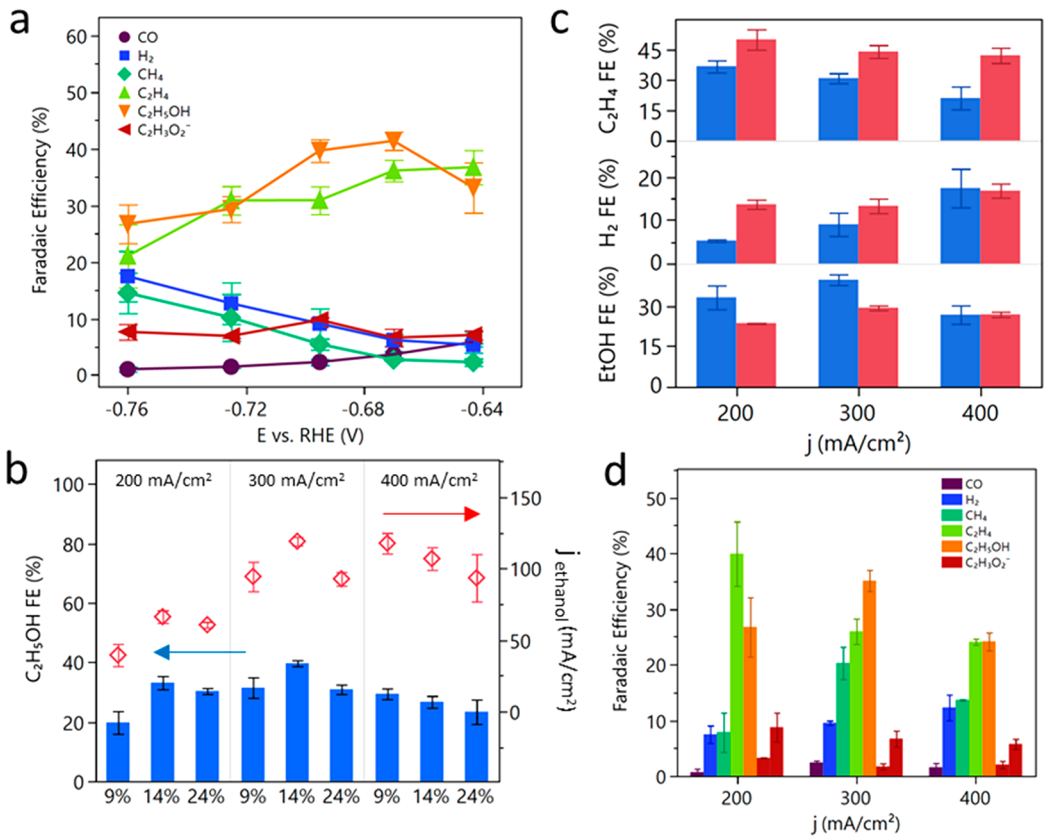

Figure 4. Electrochemical characterization of the $Ag_{0.14}/Cu_{0.86}$ catalyst. (a) Faradaic efficiency toward the major CO_2 reduction products. A few percent of formate and propanol were also detected. (b) Ethanol FE for different atomic% of Ag in the Ag/Cu catalysts and their respective partial current densities. (c) Faradaic efficiency comparison between Cu (red) and $Ag_{0.14}/Cu_{0.86}$(blue), showing change in the H_2, C_2H_4, and C_2H_5OH productions. All experiments in (a–c) were performed in 1 M KOH electrolyte. (d) The products distribution for the $Ag_{0.14}/Cu_{0.86}$ catalyst in 1 M $KHCO_3$ electrolyte.

STEM indicate a uniform distribution of Ag and Cu. The elemental Ag percentages detected using EDX were 9%, 14%, and 24% for the three different samples, which we term $Ag_{0.09}/Cu_{0.91}$, $Ag_{0.14}/Cu_{0.86}$, and $Ag_{0.24}/Cu_{0.76}$, respectively.

X-ray power diffraction (XRD) (Figure S6) reveals peak broadening consistent with ca. 50 nm crystalline grain size from a Debye–Scherrer analysis. The Cu(111) reflection in the $Ag_{0.14}/Cu_{0.86}$ sample is shifted to a lower 2θ of 42.9° compared to the pure Cu sample at 43.4°. This suggests bulk miscibility within the Ag/Cu catalyst, consistent with an alloy phase.[28] From X-ray photoelectron spectroscopy (XPS) (Figure 3d and Figure S7), Ag is mostly in the pure metallic state, while oxide is present in Cu. However, when the catalyst is studied via operando X-ray absorption near edge structure (XANES) (Figure S8) under applied negative potential, only Cu^0 is observed. We conclude that the Cu oxide seen in ex situ measurements was likely introduced by exposure to air. From the operando extended X-ray adsorption fine structure (EXAFS) data, the coordination numbers (CN) of Cu–Cu for the different Ag/Cu samples were obtained by fitting and found to equal 10.7, 10.2, and 9.6, respectively (Figure 3e and Figure S9). The gradual decrease of CN as Ag concentration increase also agrees with the view that Ag and Cu are in an alloy phase, instead of segregated Ag and Cu clusters.

Taken together, these studies indicate that the Ag/Cu catalysts do little to modulate the surface morphology, and that they exist in high uniformity throughout the bulk. This enables investigation of the binding site diversity mechanism and comparison with studies focused on intrinsic catalyst activity.

The catalysts were tested in 1 M KOH electrolyte in a flow-cell system for CO_2RR.[4,30] Gas phase products were analyzed using a gas chromatograph (GC), while liquid products were detected using nuclear magnetic resonance (NMR).

Figure 4a shows the distribution of major CO_2RR products at different potential vs reversible hydrogen electrode (RHE). For the best catalysts ($Ag_{0.14}/Cu_{0.86}$), the ethanol efficiency was 41% with a current density of 250 mA/cm^2 at −0.67 V vs RHE. The pure copper control (Figure S10), for comparison, achieved a FE of 29%.

The 41% ethanol FE reported is the highest reported for a catalyst providing current density greater than 10 mA/cm^2 (Table S1). The low overpotential for the $Ag_{0.14}/Cu_{0.86}$ catalyst led to a record cathodic energy efficiency (EE) of 25%. The ethanol FE for $Ag_{0.14}/Cu_{0.86}$ is 1.5× higher than in the previous best reports.

To investigate any role for surface morphology differences, we measured the double layer capacitance (C_{dl}) of the $Ag_{0.14}/Cu_{0.86}$ and Cu samples. We found that the electrochemical surface areas (ECSA) are the same to within 7% for Ag/Cu vs Cu controls (Figure S11). The 1.5× increase in partial current density for the $Ag_{0.14}/Cu_{0.86}$ compared to Cu is thus much larger than the small relative difference in ECSA.

Comparing product distributions for $Ag_{0.14}/Cu_{0.86}$ vs Cu controls (Figure 4c), the hydrogen and ethylene FE decrease, while ethanol FE increases, when Ag is introduced. The

DOI: 10.1021/jacs.9b02945
J. Am. Chem. Soc. XXXX, XXX, XXX–XXX

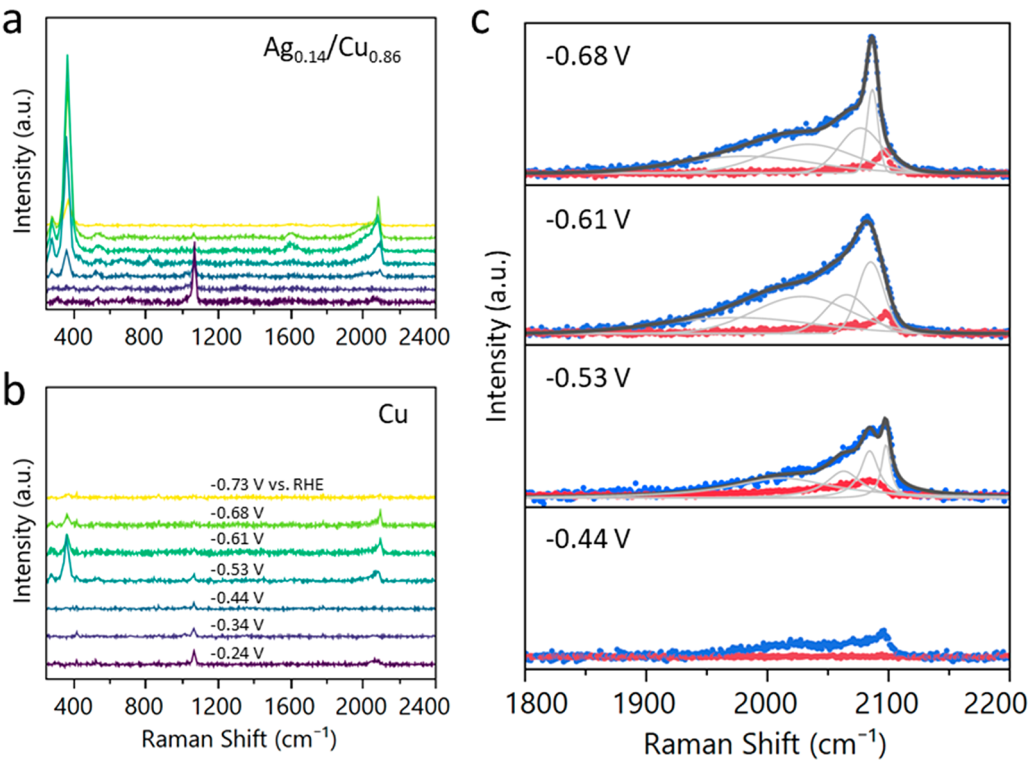

Figure 5. In situ Raman spectroscopy. In situ Raman spectroscopy for $Ag_{0.14}/Cu_{0.86}$ (a) and Cu (b) during CO_2 reduction reaction under constant potentials. (c) Zoom-in region of the CO stretching frequency for $Ag_{0.14}/Cu_{0.86}$ (blue) and Cu (red). The $Ag_{0.14}/Cu_{0.86}$ band can be deconvolved into multiple peaks to reflect the multiple binding configurations.

combined total, ethylene plus ethanol, FE for both $Ag_{0.14}/Cu_{0.86}$ and Cu are similar, in the 80% range. The switch in FE from ethylene to ethanol, without affecting the total C_2, is compatible with the view that the ethylene reaction path is destabilized, and the current is redirected to ethanol instead.

We further synthesized a layered-Ag/Cu sample, sputtering Ag and Cu sequentially instead of concurrently. Despite having similar averaged elemental composition, the layered-Ag/Cu showed a best ethanol FE at only 26% (Figure S12). This observation suggests that the high population of diverse binding sites from even distribution of Ag and Cu is required to accomplish the enhanced ethanol production.

The $Ag_{0.14}/Cu_{0.86}$ catalyst also shows excellent performance (37% FE) in neutral electrolyte (Figure 4d, 1 M $KHCO_3$). Under high current density conditions, the local pH is expected to become alkaline even in $KHCO_3$.[31,32] This explains that its performance closely approaches that in 1 M KOH.[33] The performance of the $Ag_{0.14}/Cu_{0.86}$ catalyst in neutral bulk pH is also the best reported (Table S1). The stability of the $Ag_{0.14}/Cu_{0.86}$ catalyst was tested in 1 M KOH and no decay in FE and current density was observed within 2 h (Figure S13).

In light of the switch between ethylene and ethanol FE, we investigated further the Ag/Cu and Cu catalysts to study the ethanol enhancement mechanism. CO stripping experiments (Figure S14) show that the CO desorption peak shifted from ca. 0.81 to 0.52 V vs RHE from the Cu to Ag/Cu sample. The change in potential indicates a change in the binding sites for Ag/Cu compared to Cu. Additionally, the negative shift in potential for Ag/Cu suggests a weaker binding energy, in line with the view that lowering the catalyst-carbon bonding ability should destabilize the unsaturated ethylene intermediates.

To probe the type of binding sites, we used in situ surface-enhanced Raman spectroscopy (SERS) to investigate the energetic fingerprints of the binding sites on the Cu and Ag/Cu samples (Figure 5a,b). The intensities of the spectra for Ag/Cu reside above those of Cu, a finding we attribute to the enhanced SERS signal from silver.[34] Figure 5c compares the CO stretching frequency for both Ag/Cu and Cu. The CO peak on Cu is located between 2050 to 2100 cm^{-1}, and this can be deconvolved into top-bound CO and bridge-bound CO.[35] The CO peak on Ag/Cu is observed in a much broader region, from 1900 to 2100 cm^{-1}. This is consistent with a multisite binding mechanism:[36,37] during CO adsorption onto a metal surface, electron density is donated through the CO 5σ orbital, and the electron is back-donated to the CO 2π* antibonding orbital; the strength of the electron back-donation influences the C−O bond strength, and this is manifested in the Raman spectra. Thus, with many different binding configurations on the Ag/Cu surface, each binding configuration has a different electron back-donating ability and shows up at a distinct Raman wavenumber. Overlapping a range of binding configurations can account for the broad spectrum observed in Figure 5c.

In situ Raman studies of the layered-Ag/Cu catalysts did not show the broad C−O stretching frequency (Figure S15), a finding we ascribe to the failure to implement diverse binding sites in this layered control.

We deconvolve the Raman spectra for Ag/Cu at −0.53, −0.61, and −0.68 V vs RHE and observe that at least 4 peaks are necessary to give a good fit to the experimental data. We further calculated the CO stretching frequency with DFT harmonic oscillator approximation for all the possible binding sites on the Ag/Cu model surface and confirm that the Raman peaks span a range from 1750 to 2060 cm^{-1} (Table S6). The

DOI: 10.1021/jacs.9b02945
J. Am. Chem. Soc. XXXX, XXX, XXX−XXX

excellent agreement between the simulated and experimental Raman spectra serves as further evidence that, with the introduction of Ag, the coordinated pure Cu surface is replaced with Cu neighboring Ag atoms, which leads to the multiple different binding configurations and the distinct Raman peaks. Due to the unsaturated nature of the ethylene reaction intermediates, the ethylene reaction path is suppressed and ethanol is promoted.

Taken together, the DFT calculations, the electrochemical data and the spectroscopic evidence correlate the enhanced ethanol production from the Ag/Cu catalyst with binding site diversity.

CONCLUSION

We have presented a strategy, motivated by a DFT study, to manipulate the Cu surface using a more inert element to increase the binding sites diversity and disrupt the coordination environment for intermediates on the pathway to ethylene. The best catalyst achieves 41% Faradaic efficiency and 25% energy efficiency for ethanol, the highest among reported values. Morphology characterization and in situ XAS indicate an Ag/Cu alloy phase catalyst. Electrochemical experiments and in situ Raman reveal a diversity of reaction sites that—from DFT—destabilize the ethylene reaction path. The multisite mechanism presented here provides a new direction of thinking for designing catalyst to promote ethanol. We also highlight a strategy to control the stability of reaction intermediates to tune the reaction path—a principle that could be applied to promote other value-added products from CO_2RR.

EXPERIMENTAL SECTION

DFT Calculations. In this work, we carried out all the DFT calculations with a periodic slab model using the Vienna ab initio simulation program (VASP).[38−41] The generalized gradient approximation (GGA) with the Perdew−Burke−Ernzerhof (PBE)[42] exchange-correlation functional was used. To describe the electron−ion interactions, the projector-augmented wave (PAW)[43,44] method was utilized, and the cutoff energy for the plane-wave basis set was 450 eV. In order to illustrate the long-range dispersion interactions between the adsorbates and catalysts the D3 correction method[45] by Grimme et al. was employed. Brillouin zone integration was accomplished using a 3 × 3 × 1 Monkhorst−Pack k-point mesh. The effect of solvent is considered using the implicit solvation model implemented in VASPsol.[46,47] All the adsorption geometries were optimized using a force-based conjugate gradient algorithm. For the modeling of Cu(111), the crystal structure was optimized, and Cu(111) was modeled with a periodic four-layer p(3 × 3) model with the 2 lower layers fixed and 2 upper layers relaxed.

The vibrational frequency analysis was made using the harmonic oscillator approximation with two displacements in each direction plus the ground state.

Catalyst Preparation. Ag/Cu catalysts were deposited by cosputtering with Cu and Ag targets at approximately 2 Å/s rate onto a PTFE substrate (450 nm pore with polypropylene support). The final catalysts are typically 300 nm thick. The quantities of Ag and Cu are controlled by the power applied to the respective targets during deposition. Layered-Ag/Cu was deposited by sequentially changing the targets to deposit 15 nm Ag followed by 85 nm Cu and repeating three times. Pure Cu catalyst was deposited similarly without the Ag target.

Structure and Composition Characterizations. Morphologies of the catalysts were examined with Hitachi S5000 field emission scanning electron microscopy and Hitachi HF-3300 transmission scanning microscopy, both equipped with a Bruker energy dispersive X-ray spectroscopy detector. Rigaku (Miniflex 600 6G) diffractometer was used to collect the XRD patterns with Cu kα X-ray as the radiation source. Oxidation state and surface composition information was analyzed with ThermoFisher Scientific K-Alpha photoelectron spectroscopy using Al Kα X-ray radiation. XPS spectra was calibrated with C 1s peak at 284.5 eV. In situ XAS data was collected at the 9BM beamline of the Advanced Photon Source Advanced Photon Source (APS) located in the Argonne National Laboratory.

In situ Raman spectroscopy was carried out with a Renishaw inVia Raman spectrometer in an in-house in situ flow cell and a 50× water immersion lens. Pt wire and Ag/AgCl were used as the counter and reference electrode, respectively. As-prepared Ag/Cu or Cu catalyst was used as the working electrode with 1 M KOH electrolyte and continuous CO_2 flowing on the backside.

Electrochemical Performances. Electrochemical data was collected with an Autolab PGSTAT204 potentiostat in a flow cell reactor. Either 1 M KOH or 1 M $KHCO_3$ was used as the catholyte, 1 M KOH was used as the anolyte and an anion exchanged membrane (Fumasep FAA-3-PK-130) was used to separate the two electrodes. All potentials were measured with a saturated Ag/AgCl electrode and converted to RHE scale according to $E_{RHE} = E_{Ag/AgCl} + 0.197 + 0.059 \times pH$. The series resistance of the electrolyte was determined by electrochemical impedance spectroscopy with frequency ranges from 10^5 to 1 Hz and 20 mV amplitude. During the reaction, gas phase products were quantified with gas chromatography (PerkinElmer Clarus 600), equipped with a thermal conductivity detector and a flame ionization detector. Liquid products were quantified with a 600 MHz Agilent DD2 ^{1}H NMR spectrometer with water suppression. Liquid samples were all collected after the reaction had run for 20 min. D_2O and DMSO were added to the liquid sample as lock solvent and internal reference, respectively. C_{dl} was determined by running the catalysts at a non-Faradaic region at 10, 20, 50, 75, 100 mV/s scan rate and fitting the charging current linearly.

ASSOCIATED CONTENT

Supporting Information

The Supporting Information is available free of charge on the ACS Publications website at DOI: 10.1021/jacs.9b02945.

CIF files for all the structures considered in the DFT studies (ZIP)

Computational details, Table S1−S6, Figures S1−S15 (PDF)

AUTHOR INFORMATION

Corresponding Author

*ted.sargent@utoronto.ca

ORCID

Yuguang C. Li: 0000-0002-9559-7051
Ziyun Wang: 0000-0002-2817-8367
Dae-Hyun Nam: 0000-0002-0871-1355
Fengwang Li: 0000-0003-1531-2966
Cao-Thang Dinh: 0000-0001-9641-9815
Oleksandr Voznyy: 0000-0002-8656-5074
David Sinton: 0000-0003-2714-6408
Edward H. Sargent: 0000-0003-0396-6495

Author Contributions

‖Y.C.L. and Z.W. contributed equally.

Notes

The authors declare no competing financial interest.

ACKNOWLEDGMENTS

The authors would like to acknowledge funding supporting from Suncor Energy, the Ontario Research fund, and the Natural Sciences and Engineering Research Council (NSERC). All DFT computations were performed on the

DOI: 10.1021/jacs.9b02945
J. Am. Chem. Soc. XXXX, XXX, XXX−XXX

IBM BlueGene/Q supercomputer with support from the Southern Ontario Smart Computing Innovation Platform (SOSCIP). SOSCIP is funded by the Federal Economic Development Agency of Southern Ontario, the Province of Ontario, IBM Canada, Ontario Centres of Excellence, Mitacs and 15 Ontario academic member institutions. This research was enabled inpart by support provided by Compute Ontario and Compute Canada. This research used synchrotron resources of the Advanced Photon Source (APS), an Office of Science User Facility operated for the U.S. Department of Energy (DOE) Office of Science by Argonne National Laboratory, and was supported by the U.S. DOE under Contract No. DE-AC02-06CH11357, and the Canadian Light Source and its funding partners. The authors thank Dr. T. P. Wu, Dr. Z. Finfrock, Dr. G. Sterbinsky, and Dr. L. Ma for technical support at the 9BM beamline of the Advanced Photon Source. D.S. acknowledges the NSERC E.W.R. Steacie Memorial Fellowship. J.L. acknowledges the Banting Post-doctoral Fellowships program.

REFERENCES

(1) García de Arquer, F. P.; Bushuyev, O. S.; De Luna, P.; Dinh, C.-T.; Seifitokaldani, A.; Saidaminov, M. I.; Tan, C.-S.; Quan, L. N.; Proppe, A.; Kibria, M. G.; Kelley, S. O.; Sinton, D.; Sargent, E. H. 2D metal oxyhalide-derived catalysts for efficient CO_2 electroreduction. *Adv. Mater.* **2018**, *30* (38), 1802858.

(2) Liu, M.; Pang, Y.; Zhang, B.; De Luna, P.; Voznyy, O.; Xu, J.; Zheng, X.; Dinh, C. T.; Fan, F.; Cao, C.; de Arquer, F. P. G.; Safaei, T. S.; Mepham, A.; Klinkova, A.; Kumacheva, E.; Filleter, T.; Sinton, D.; Kelley, S. O.; Sargent, E. H. Enhanced electrocatalytic CO_2 reduction via field-induced reagent concentration. *Nature* **2016**, *537*, 382.

(3) Jouny, M.; Luc, W.; Jiao, F. General techno-economic analysis of CO_2 electrolysis systems. *Ind. Eng. Chem. Res.* **2018**, *57* (6), 2165−2177.

(4) Dinh, C. T.; Burdyny, T.; Kibria, M. G.; Seifitokaldani, A.; Gabardo, C. M.; García de Arquer, F. P.; Kiani, A.; Edwards, J. P.; De Luna, P.; Bushuyev, O. S.; Zou, C.; Quintero-Bermudez, R.; Pang, Y.; Sinton, D.; Sargent, E. H. CO_2 electroreduction to ethylene via hydroxide-mediated copper catalysis at an abrupt interface. *Science* **2018**, *360* (6390), 783.

(5) Hori, Y.; Murata, A.; Takahashi, R. Formation of hydrocarbons in the electrochemical reduction of carbon dioxide at a copper electrode in aqueous solution. *J. Chem. Soc., Faraday Trans. 1* **1989**, *85* (8), 2309−2326.

(6) Kuhl, K. P.; Cave, E. R.; Abram, D. N.; Jaramillo, T. F. New insights into the electrochemical reduction of carbon dioxide on metallic copper surfaces. *Energy Environ. Sci.* **2012**, *5* (5), 7050−7059.

(7) Lv, K.; Fan, Y.; Zhu, Y.; Yuan, Y.; Wang, J.; Zhu, Y.; Zhang, Q. Elastic Ag-anchored N-doped graphene/carbon foam for the selective electrochemical reduction of carbon dioxide to ethanol. *J. Mater. Chem. A* **2018**, *6* (12), 5025−5031.

(8) Yanming, L.; Yujing, Z.; Kai, C.; Xie, Q.; Xinfei, F.; Yan, S.; Shuo, C.; Huimin, Z.; Yaobin, Z.; Hongtao, Y.; R, H. M. Selective electrochemical reduction of carbon dioxide to ethanol on a boron- and nitrogen-Co-doped nanodiamond. *Angew. Chem., Int. Ed.* **2017**, *56* (49), 15607−15611.

(9) Clark, E. L.; Hahn, C.; Jaramillo, T. F.; Bell, A. T. Electrochemical CO_2 reduction over compressively strained CuAg surface alloys with enhanced multi-carbon oxygenate selectivity. *J. Am. Chem. Soc.* **2017**, *139* (44), 15848−15857.

(10) Hoang, T. T. H.; Verma, S.; Ma, S.; Fister, T. T.; Timoshenko, J.; Frenkel, A. I.; Kenis, P. J. A.; Gewirth, A. A. Nanoporous copper−silver alloys by additive-controlled electrodeposition for the selective electroreduction of CO_2 to ethylene and ethanol. *J. Am. Chem. Soc.* **2018**, *140* (17), 5791−5797.

(11) Lee, S.; Park, G.; Lee, J. Importance of Ag−Cu biphasic boundaries for selective electrochemical reduction of CO_2 to ethanol. *ACS Catal.* **2017**, *7* (12), 8594−8604.

(12) Lum, Y.; Cheng, T.; Goddard, W. A.; Ager, J. W. Electrochemical CO reduction builds solvent water into oxygenate products. *J. Am. Chem. Soc.* **2018**, *140* (30), 9337−9340.

(13) Calle-Vallejo, F.; Koper, M. T. M. Theoretical considerations on the electroreduction of CO to C2 species on Cu(100) Electrodes. *Angew. Chem., Int. Ed.* **2013**, *52* (28), 7282−7285.

(14) Kortlever, R.; Shen, J.; Schouten, K. J. P.; Calle-Vallejo, F.; Koper, M. T. M. Catalysts and reaction pathways for the electrochemical reduction of carbon dioxide. *J. Phys. Chem. Lett.* **2015**, *6* (20), 4073−4082.

(15) Handoko, A. D.; Chan, K. W.; Yeo, B. S. $-CH_3$ mediated pathway for the electroreduction of CO_2 to ethane and ethanol on thick oxide-derived copper catalysts at low overpotentials. *ACS Energy Lett.* **2017**, *2* (9), 2103−2109.

(16) Hahn, C.; Hatsukade, T.; Kim, Y.-G.; Vailionis, A.; Baricuatro, J. H.; Higgins, D. C.; Nitopi, S. A.; Soriaga, M. P.; Jaramillo, T. F. Engineering Cu surfaces for the electrocatalytic conversion of CO_2: Controlling selectivity toward oxygenates and hydrocarbons. *Proc. Natl. Acad. Sci. U. S. A.* **2017**, *114* (23), 5918−5923.

(17) Ren, D.; Ang, B. S.-H.; Yeo, B. S. Tuning the selectivity of carbon dioxide electroreduction toward ethanol on oxide-derived Cu_xZn catalysts. *ACS Catal.* **2016**, *6* (12), 8239−8247.

(18) Morales-Guio, C. G.; Cave, E. R.; Nitopi, S. A.; Feaster, J. T.; Wang, L.; Kuhl, K. P.; Jackson, A.; Johnson, N. C.; Abram, D. N.; Hatsukade, T.; Hahn, C.; Jaramillo, T. F. Improved CO_2 reduction activity towards C2+ alcohols on a tandem gold on copper electrocatalyst. *Nat. Catal.* **2018**, *1* (10), 764−771.

(19) Chi, D.; Yang, H.; Du, Y.; Lv, T.; Sui, G.; Wang, H.; Lu, J. Morphology-controlled CuO nanoparticles for electroreduction of CO_2 to ethanol. *RSC Adv.* **2014**, *4* (70), 37329−37332.

(20) Manthiram, K.; Beberwyck, B. J.; Alivisatos, A. P. Enhanced electrochemical methanation of carbon dioxide with a dispersible nanoscale copper catalyst. *J. Am. Chem. Soc.* **2014**, *136* (38), 13319−13325.

(21) Duan, Y.-X.; Meng, F.-L.; Liu, K.-H.; Yi, S.-S.; Li, S.-J.; Yan, J.-M.; Jiang, Q. Amorphizing of Cu nanoparticles toward highly efficient and robust electrocatalyst for CO_2 reduction to liquid fuels with high Faradaic efficiencies. *Adv. Mater.* **2018**, *30* (14), 1706194.

(22) Zhuang, T.-T.; Liang, Z.-Q.; Seifitokaldani, A.; Li, Y.; De Luna, P.; Burdyny, T.; Che, F.; Meng, F.; Min, Y.; Quintero-Bermudez, R.; Dinh, C. T.; Pang, Y.; Zhong, M.; Zhang, B.; Li, J.; Chen, P.-N.; Zheng, X.-L.; Liang, H.; Ge, W.-N.; Ye, B.-J.; Sinton, D.; Yu, S.-H.; Sargent, E. H. Steering post-C−C coupling selectivity enables high efficiency electroreduction of carbon dioxide to multi-carbon alcohols. *Nat. Catal.* **2018**, *1* (6), 421−428.

(23) Andrews, E.; Ren, M.; Wang, F.; Zhang, Z.; Sprunger, P.; Kurtz, R.; Flake, J. Electrochemical reduction of CO_2 at Cu nanocluster/(1010) ZnO electrodes. *J. Electrochem. Soc.* **2013**, *160* (11), H841−H846.

(24) Cheng, T.; Xiao, H.; Goddard, W. A. Full atomistic reaction mechanism with kinetics for CO reduction on Cu(100) from ab initio molecular dynamics free-energy calculations at 298 K. *Proc. Natl. Acad. Sci. U. S. A.* **2017**, *114*, 201612106.

(25) Wang, L.; Nitopi, S. A.; Bertheussen, E.; Orazov, M.; Morales-Guio, C. G.; Liu, X.; Higgins, D. C.; Chan, K.; NØrskov, J. K.; Hahn, C.; Jaramillo, T. F. Electrochemical carbon monoxide reduction on polycrystalline copper: effects of potential, pressure, and pH on selectivity toward multicarbon and oxygenated products. *ACS Catal.* **2018**, *8* (8), 7445−7454.

(26) Liu, X.; Xiao, J.; Peng, H.; Hong, X.; Chan, K.; NØrskov, J. K. Understanding trends in electrochemical carbon dioxide reduction rates. *Nat. Commun.* **2017**, *8*, 15438.

(27) NØrskov, J. K.; Rossmeisl, J.; Logadottir, A.; Lindqvist, L.; Kitchin, J. R.; Bligaard, T.; Jónsson, H. Origin of the overpotential for oxygen reduction at a fuel-cell cathode. *J. Phys. Chem. B* **2004**, *108* (46), 17886−17892.

DOI: 10.1021/jacs.9b02945
J. Am. Chem. Soc. XXXX, XXX, XXX−XXX

(28) Higgins, D.; Landers, A. T.; Ji, Y.; Nitopi, S.; Morales-Guio, C. G.; Wang, L.; Chan, K.; Hahn, C.; Jaramillo, T. F. Guiding electrochemical carbon dioxide reduction toward carbonyls using copper silver thin films with interphase miscibility. *ACS Energy Lett.* **2018**, *3* (12), 2947−2955.
(29) Dinh, C.-T.; García de Arquer, F. P.; Sinton, D.; Sargent, E. H. High rate, selective, and stable electroreduction of CO_2 to CO in basic and neutral media. *ACS Energy Lett.* **2018**, *3* (11), 2835−2840.
(30) Ma, S.; Luo, R.; Gold, J. I.; Yu, A. Z.; Kim, B.; Kenis, P. J. A. Carbon nanotube containing Ag catalyst layers for efficient and selective reduction of carbon dioxide. *J. Mater. Chem. A* **2016**, *4* (22), 8573−8578.
(31) Varela, A. S.; Kroschel, M.; Reier, T.; Strasser, P. Controlling the selectivity of CO_2 electroreduction on copper: The effect of the electrolyte concentration and the importance of the local pH. *Catal. Today* **2016**, *260*, 8−13.
(32) Raciti, D.; Mao, M.; Park, J. H.; Wang, C. Local pH effect in the CO_2 reduction reaction on high-surface-area copper electrocatalysts. *J. Electrochem. Soc.* **2018**, *165* (10), F799−F804.
(33) Singh, M. R.; Goodpaster, J. D.; Weber, A. Z.; Head-Gordon, M.; Bell, A. T. Mechanistic insights into electrochemical reduction of CO_2 over Ag using density functional theory and transport models. *Proc. Natl. Acad. Sci. U. S. A.* **2017**, *114* (42), E8812−E8821.
(34) Panneerselvam, R.; Liu, G.-K.; Wang, Y.-H.; Liu, J.-Y.; Ding, S.-Y.; Li, J.-F.; Wu, D.-Y.; Tian, Z.-Q. Surface-enhanced Raman spectroscopy: bottlenecks and future directions. *Chem. Commun.* **2018**, *54* (1), 10−25.
(35) Deng, Y.; Yeo, B. S. Characterization of electrocatalytic water splitting and CO_2 reduction reactions using in situ/operando Raman spectroscopy. *ACS Catal.* **2017**, *7* (11), 7873−7889.
(36) Blyholder, G. Molecular orbital view of chemisorbed carbon monoxide. *J. Phys. Chem.* **1964**, *68* (10), 2772−2777.
(37) Aizawa, H.; Tsuneyuki, S. First-principles study of CO bonding to Pt(111): validity of the Blyholder model. *Surf. Sci.* **1998**, *399* (2), L364−L370.
(38) Kresse, G.; Hafner, J. Ab initio molecular-dynamics simulation of the liquid-metal–amorphous-semiconductor transition in germanium. *Phys. Rev. B: Condens. Matter Mater. Phys.* **1994**, *49* (20), 14251−14269.
(39) Kresse, G.; Hafner, J. Ab initio molecular dynamics for liquid metals. *Phys. Rev. B: Condens. Matter Mater. Phys.* **1993**, *47* (1), 558−561.
(40) Kresse, G.; Furthmüller, J. Efficiency of ab-initio total energy calculations for metals and semiconductors using a plane-wave basis set. *Comput. Mater. Sci.* **1996**, *6* (1), 15−50.
(41) Kresse, G.; Furthmüller, J. Efficient iterative schemes for ab initio total-energy calculations using a plane-wave basis set. *Phys. Rev. B: Condens. Matter Mater. Phys.* **1996**, *54* (16), 11169−11186.
(42) Perdew, J. P.; Burke, K.; Ernzerhof, M. Generalized gradient approximation made simple. *Phys. Rev. Lett.* **1996**, *77* (18), 3865−3868.
(43) Kresse, G.; Joubert, D. From ultrasoft pseudopotentials to the projector augmented-wave method. *Phys. Rev. B: Condens. Matter Mater. Phys.* **1999**, *59* (3), 1758−1775.
(44) Blöchl, P. E. Projector augmented-wave method. *Phys. Rev. B: Condens. Matter Mater. Phys.* **1994**, *50* (24), 17953−17979.
(45) Grimme, S.; Antony, J.; Ehrlich, S.; Krieg, H. A consistent and accurate ab initio parametrization of density functional dispersion correction (DFT-D) for the 94 elements H-Pu. *J. Chem. Phys.* **2010**, *132* (15), 154104.
(46) Mathew, K.; Hennig, R. G. Implicit self-consistent description of electrolyte in plane-wave density-functional theory arXiv: 1601.03346, 2016.
(47) Mathew, K.; Sundararaman, R.; Letchworth-Weaver, K.; Arias, T. A.; Hennig, R. G. Implicit solvation model for density-functional study of nanocrystal surfaces and reaction pathways. *J. Chem. Phys.* **2014**, *140* (8), 084106.

DOI: 10.1021/jacs.9b02945
J. Am. Chem. Soc. XXXX, XXX, XXX−XXX